J. Fluid Mech. (2008), *vol.* 607, *pp.* 119–139.
doi:10.1017/S0022112008001882 Printed in the United Kingdom

Torsional oscillations of the large-scale circulation in turbulent Rayleigh–Bénard convection

DENIS FUNFSCHILLING†, ERIC BROWN‡ AND GUENTER AHLERS

Department of Physics and iQCD, University of California, Santa Barbara, CA 93106, USA

(Received 8 May 2007 and in revised form 28 March 2008)

Measurements over the Rayleigh-number range $10^8 \lesssim R \lesssim 10^{11}$ and Prandtl-number range $4.4 \lesssim \sigma \lesssim 29$ that determine the torsional nature and amplitude of the oscillatory mode of the large-scale circulation (LSC) of turbulent Rayleigh–Bénard convection are presented. For cylindrical samples of aspect ratio $\Gamma = 1$ the mode consists of an azimuthal twist of the near-vertical LSC circulation plane, with the top and bottom halves of the plane oscillating out of phase by half a cycle. The data for $\Gamma = 1$ and $\sigma = 4.4$ showed that the oscillation amplitude varied irregularly in time, yielding a Gaussian probability distribution centred at zero for the displacement angle. This result can be described well by the equation of motion of a stochastically driven damped harmonic oscillator. It suggests that the existence of the oscillations is a consequence of the stochastic driving by the small-scale turbulent background fluctuations of the system, rather than a consequence of a Hopf bifurcation of the deterministic system. The power spectrum of the LSC orientation had a peak at finite frequency with a quality factor $Q \simeq 5$, nearly independent of R. For samples with $\Gamma \geqslant 2$ we did not find this mode, but there remained a characteristic periodic signal that was detectable in the area density ρ_p of the plumes above the bottom-plate centre. Measurements of ρ_p revealed a strong dependence on the Rayleigh number R, and on the aspect ratio Γ that could be represented by $\rho_p \sim \Gamma^{2.7\pm0.3}$. Movies are available with the online version of the paper.

1. Introduction

Understanding turbulent Rayleigh–Bénard convection (RBC) in a fluid heated from below (see, for instance, Siggia 1994; Kadanoff 2001; Ahlers, Grossmann & Lohse 2002) remains one of the challenging problems in nonlinear physics. It is well established that a major component of the dynamics of this system is a large-scale circulation (LSC) (Sano, Wu & Libchaber 1989; Castaing *et al.* 1989; Ciliberto, Cioni & Laroche 1996; Qiu & Tong 2001*a*; Funfschilling & Ahlers 2004; Sun, Xia & Tong 2005*b*; Tsuji *et al.* 2005). The LSC plays an important role in many natural phenomena, including atmospheric and oceanic convection (see, for instance, van Doorn *et al.* 2000) where it has an impact on climate, and convection in the outer core of Earth (see, for instance, Glatzmaier, Coe & Roberts 1999) where it is responsible for the generation of the magnetic field.

† Present address: LSGC CNRS – GROUPE ENSIC, BP 451, 54001 Nancy Cedex, France.
‡ Present address: The James Franck Institute and Department of Physics, The University of Chicago, Chicago, IL 60637, USA.

In this paper we consider cylindrical samples, primarily with aspect ratio $\Gamma \equiv D/L \simeq 1$ (D is the diameter and L the height). For these the LSC consists of a single convection roll, with both downflow and upflow near the sidewall but at azimuthal locations θ that differ by π. An interesting property of the LSC is a twisting azimuthal oscillation mode with frequency $f_0 = \omega_0/2\pi$, where ω_0 is the angular oscillation frequency. The spatial nature of this mode has become apparent only recently (Funfschilling & Ahlers 2004; Resagk *et al.* 2006; Xi, Zhou & Xia 2006). It is a time-periodic twist of the circulation plane of the LSC that consists, at a given moment, of a rotation in opposite azimuthal directions in the top and the bottom half of the sample (Funfschilling & Ahlers 2004). In the present paper the existence of this mode is confirmed by quite different measurements, its spatio-temporal structure is further illuminated, and measurements of its properties are extended to a larger Rayleigh- and Prandtl-number range.

Although the geometrical features of this mode were unclear until recently, a characteristic frequency was measured much earlier in a number of single-point determinations of the temperature or the velocity (Heslot, Castaing & Libchaber 1987; Castaing *et al.* 1989; Ciliberto *et al.* 1996; Takeshita *et al.* 1996; Cioni, Ciliberto & Sommeria 1997; Qiu, Yao & Tong 2000; Qiu & Tong 2001*a*, *b*; Niemela *et al.* 2001; Qiu & Tong 2002; Qiu *et al.* 2004). Depending on the nature of the probe, and the probe location within the sample, such measurements could determine either the inverse turnover time $1/\mathscr{T}$ of the LSC or its azimuthal oscillation frequency f_0. In either case, it was found that, within experimental resolution, f_0 is equal to $1/\mathscr{T}$ over a wide parameter range (Qiu & Tong 2002; Funfschilling & Ahlers 2004; Brown, Funfschilling & Ahlers 2007). The reason for this equality is not known at this time.

Consistent with the twisting nature of the mode, we detected no oscillations in the orientation θ_0 of the circulation plane at the horizontal mid-plane of the sample. Instead, θ_0 revealed a random time dependence that could be described well by azimuthal diffusion (Brown, Nikolaenko & Ahlers 2005*a*; Sun, Xi & Xia 2005*a*; Brown & Ahlers 2006*b*; Xi *et al.* 2006), interrupted occasionally by larger re-orientations, as discussed before (Brown *et al.* 2005*a*; Brown & Ahlers 2006*b*; Xi *et al.* 2006). The out-of-phase oscillations were found in the angles θ_t and θ_b measured at vertical positions $L/4$ above and below the mid-plane respectively. Whereas a purely periodic oscillation with characteristic amplitude A should yield probability-distribution functions $p_{\theta_b'}$ of $\theta_b' = \theta_b - \theta_0$ and $p_{\theta_t'}$ of $\theta_t' = \theta_t - \theta_0$ with pronounced peaks at angles close to $\pm A$, we found that $p_{\theta_b'}$ and $p_{\theta_t'}$ were Gaussian distributed about $\theta_b' = 0$ or $\theta_t' = 0$. Such a distribution can be reproduced by a damped harmonic oscillator driven by white noise (see, for instance, Gitterman 2005). Thus the measurements suggest that the existence of the oscillatory mode is a consequence of the stochastic driving by the small-scale turbulent background fluctuations, and that it is not a consequence of a Hopf bifurcation of the deterministic system.

Consistent with the conclusions of the previous paragraph, we found that the oscillatory mode has oscillating but gradually decaying time-correlation functions and a Lorentzian peak in the height-dependent power spectrum (or structure factor) $S(z, f)$ of the LSC orientation $\theta(z, t)$. For $\Gamma = 1$ and Prandtl number $\sigma = 4.4$ we present results for the height S_0, centre frequency f_0, half-width σ_f, and total power $P = \pi\sigma_f S_0$ of this peak as a function of the Rayleigh number

$$R = \frac{\alpha g \Delta T L^3}{\kappa \nu} \tag{1.1}$$

(α is the isobaric thermal expansion coefficient, g the acceleration due to gravity, and ΔT the applied temperature difference). Although the half-width increases with R, the centre frequency increases also with the result that the quality factor $Q = f_0/(2\sigma_f) \simeq 5$ remains nearly independent of R. This suggests that the oscillations will survive up to values of R well above those available in the laboratory, unless a dramatic event (such as the disappearance of the LSC itself) intervenes and invalidates a simple power-law extrapolation of the R-dependences of f_0 and σ_f.

We find that the oscillatory mode exists only for aspect ratios near one. For larger Γ we do not find the azimuthal oscillation, but instead observe that the plume area density above the centre portion of the bottom plate oscillates periodically. Thus, as the aspect ratio changes, the nature of the time-periodic mode of the LSC changes its character.

2. Experimental apparatus and methods

2.1. *The samples*

Measurements using water at a mean temperature of 40°C (Prandtl number $\sigma \equiv \nu/\kappa = 4.38$ and $\nu = 6.7 \times 10^{-7}\,\mathrm{m^2\,s^{-1}}$) as the fluid were made for the two cylindrical samples with $\Gamma \simeq 1$ described by Brown *et al.* (2005*b*) as the 'medium' and the 'large' sample. The top and bottom plates of both were made of copper. The Plexiglas sidewall had a thickness of 0.32 (0.63) cm for the medium (large) sample. The samples had $L(D) = 24.76$ (24.81) and 50.61 (49.69) cm respectively. Rayleigh numbers were determined from temperature measurements with five thermometers imbedded in each of the top and bottom plates.

Measurements using methanol with $\sigma = 6.0$ and $\nu = 5.79 \times 10^{-7}\,\mathrm{m^2\,s^{-1}}$ or 2-propanol with $\sigma = 28.9$ and $\nu = 1.77 \times 10^{-6}\,\mathrm{m^2\,s^{-1}}$ as the fluid were made in three smaller cylindrical samples. They each had a 6.35 mm thick aluminium bottom plate with a mirror top surface and a 3.15 mm thick sapphire top plate. A high-density polyethylene sidewall was sealed to the top and bottom plates by ethylenepropylene O-rings. One of the smaller samples had $\Gamma \simeq 1$ with $L\ (D) = 8.74$ (8.66) and had been used before by Xu *et al.* (2000) and by Funfschilling & Ahlers (2004). We shall call it the 'small' sample. The other two had $L\ (D) = 4.48$ (8.97) and 3.00 (8.96) cm respectively. They will be referred to as the $\Gamma \simeq 2$ and $\Gamma \simeq 3$ sample respectively. The bottom-plate temperature was determined with several thermistors imbedded in the plate. The top temperature was inferred from measurements of the temperature of the bath that circulated above the top sapphire plate.

2.2. *Sidewall-temperature measurements*

For the medium and large sample, three sets of eight thermistors each, equally spaced around the circumference at the three vertical positions $-L/4$, 0, and $L/4$ (we take the origin of the vertical axis at the horizontal mid-plane of the sample) and labelled $i = 0, \ldots, 7$, etc. as shown in figure 1, were imbedded in small holes drilled horizontally into but not penetrating the sidewall. The thermistors were able to sense the adjacent fluid temperature without interfering with delicate fluid-flow structures. We measured the temperature of each thermistor with a sampling period of about 2.5 s. Since the LSC carried warm (cold) fluid from the bottom (top) plate up (down) the sidewall, these thermistors detected the location of the upflow (downflow) of the LSC by indicating a relatively high (low) temperature.

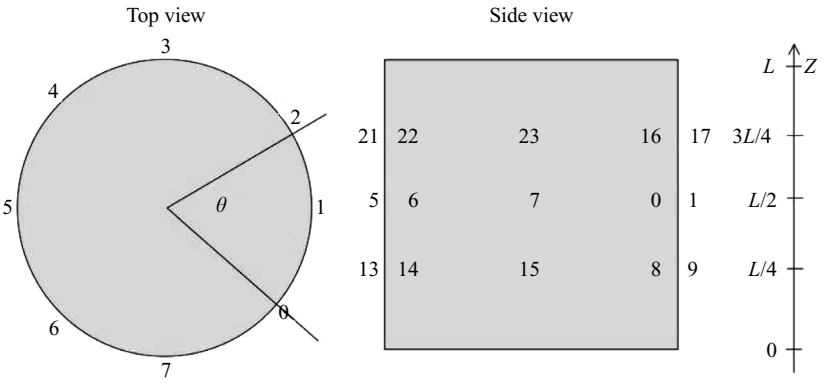

FIGURE 1. The location of the sidewall thermometers. For the top view only the thermometer locations for the set located a distance $L/2$ above the bottom plate (on the horizontal mid-plane, or $z=0$) are shown. The side view indicates the location of all three sets.

To determine the orientation and strength of the LSC, we fitted the function

$$T_i = T_0 + \delta \cos\left(\frac{i\pi}{4} - \theta_0\right), \quad i = 0, \ldots, 7, \tag{2.1}$$

separately at each time step, to the eight temperature readings obtained from the thermistors at height 0. The fit parameter δ is a measure of the temperature amplitude of the LSC and θ_0 is the azimuthal orientation of the plane of the LSC circulation. As defined here, the orientation θ_0 is on the side of the sample where the LSC is warm and upflowing and is measured relative to the location of thermometer zero. We calculated orientations θ_t and θ_b and amplitudes δ_t and δ_b for the top and bottom levels at $L/4$ and $-L/4$ separately by the same method as for the middle row. Results from this method of determining the orientation and strength of the LSC have been reported in several previous publications (Brown *et al.* 2005*a*; Ahlers, Brown & Nikolaenko 2005; Brown & Ahlers 2006*a*, *b*)

2.3. *Shadowgraph measurements*

For the small, $\Gamma \simeq 2$ and $\Gamma \simeq 3$ samples the LSC movement and plume area density close to but above (below) the bottom (top) plate were examined by means of shadowgraph images (de Bruyn *et al.* 1996) as described in part already by Funfschilling & Ahlers (2004). Figure 2(*a*) shows a typical image obtained for the small sample. This image had a background image taken with $\Delta T = 0$ subtracted, and the ratio was re-scaled to cover a suitable grey range. An elongated narrow dark stripe such as the one near the upper right of the image corresponds to a stripe of relatively warm fluid. For most of our work the optics was adjusted so as to emphasize the relatively warm plumes near the bottom plate. Cold plumes near the top plate are also discernible in the figure, but provide a relatively weaker bright signal. The two types of plumes are readily separated by image processing.

When the sample axis is parallel to the gravitational acceleration, the LSC orientation θ_0 meanders nearly randomly in the azimuthal direction (Sun *et al.* 2005*a*, Brown & Ahlers 2006*a*, *b*; Xi *et al.* 2006) on time scales much longer than the oscillation period. Some measurements were made under these conditions, but for others the sample was tilted by an angle $\beta \simeq 1^\circ$ relative to gravity. This led to a strongly preferred azimuthal orientation of the LSC circulation-plane (Ahlers *et al.* (2005); Brown *et al.* (2005*a*); Brown & Ahlers 2006*b*). In figure 3 the coordinate

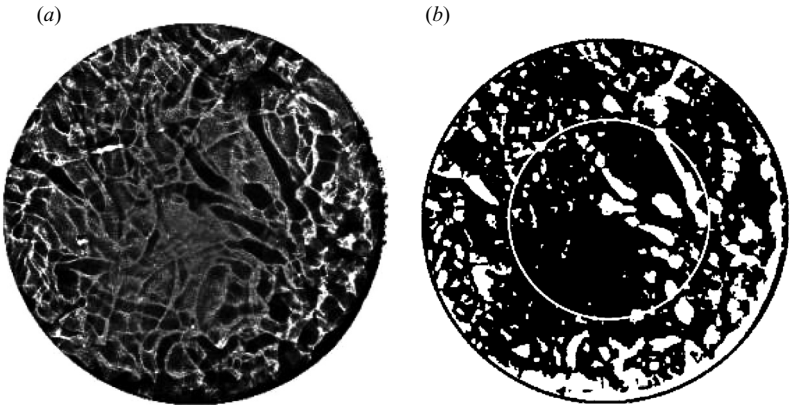

FIGURE 2. (*a*) Background-image-divided shadowgraph image of the small sample ($\Gamma = 1$) with 2-propanol at a mean temperature of 40°C. The Rayleigh number was $R = 7.8 \times 10^8$. (*b*) A binary rendering of the image in (*a*) obtained by applying a threshold and inverting the grey scale. The white circle illustrates the area used for the plume area-density measurements.

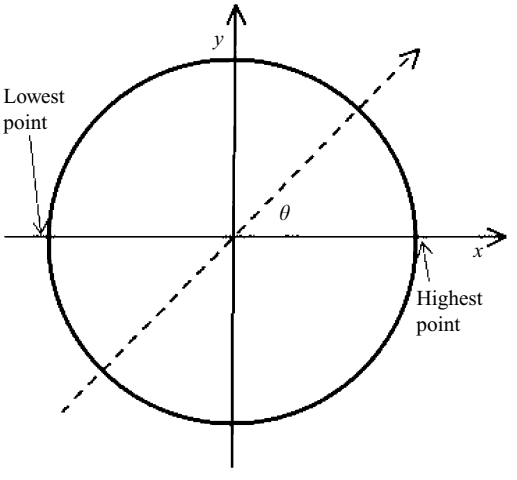

FIGURE 3. Schematic illustration of the coordinates used when the sample was tilted by an angle $\beta \simeq 1^\circ$ relative to gravity.

system relative to the tilt direction is illustrated. For the small tilt angle used the shadowgraph measurements did not resolve any influence of the tilt on the properties of the oscillatory mode.

2.3.1. *Plume-velocity measurements*

For the small sample ($\Gamma = 1$) the speed s_p and direction θ_p of the plume motion was determined from spatial cross-correlation functions

$$C(\delta \boldsymbol{r}, t) = \langle I(\boldsymbol{r}, t) I(\boldsymbol{r} + \delta \boldsymbol{r}, t + \delta t) \rangle$$

between two images separated in time by an interval δt. Here $\boldsymbol{r}$ is the two-dimensional position vector, t the time, and $\langle \ldots \rangle$ indicates a spatial average. The method is illustrated in figure 4. Two images separated in time by $\delta t = 0.9$ s (*a* and *b*) are shown. Each contains a dominant highly elongated plume. To a good approximation the plume moves in the direction of its long axis. This alignment of plumes by a shear

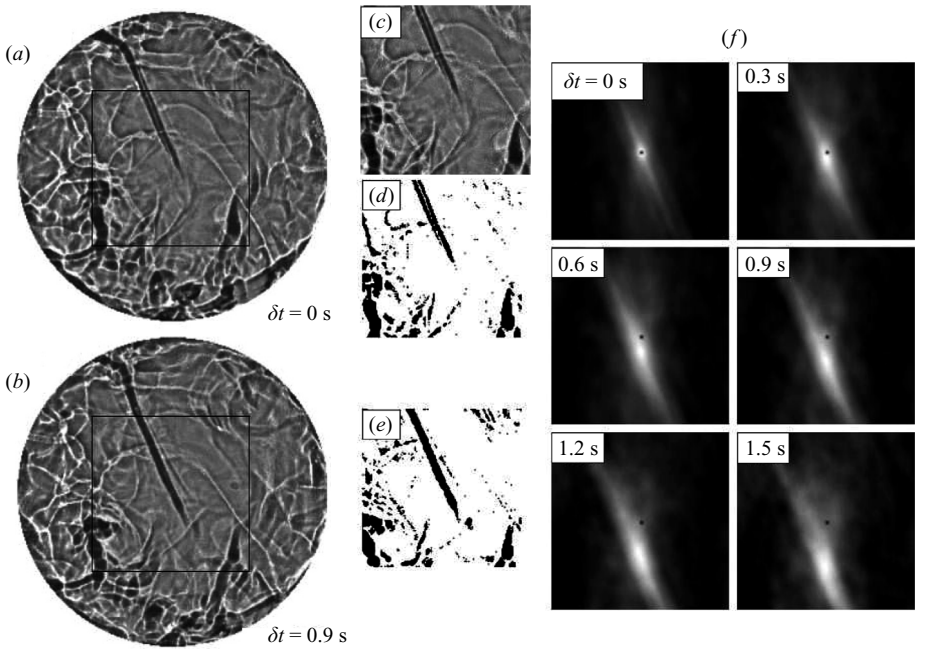

FIGURE 4. (a,b) Two background subtracted and re-scaled shadowgraph images separated in time by $\delta t = 0.9$ s. (c) A central square section of (a). (d,e) One-bit rendering of the square sections from (a) and (b). (f) Spatial cross-correlation functions between images such as (d) and (e), with several different time delays δt ranging from zero to 1.5 s (the origin is indicated by a small black dot). The fluid was methanol at a mean temperature of 40°C and $R = 4.6 \times 10^8$.

flow is a well-known phenomenon and consistent with stability analysis for convection rolls in the presence of shear (Kelly 1994).

A central square (figure 4c) was extracted and converted to a one-bit image showing the plumes as black and most of the rest of the sample as white (figure 4d,e). The cross-correlation function between two such central squares, separated in time by various values indicated in the figure, are shown in figure 4(f). For $\delta t = 0$ s there is the auto-correlation function which has a maximum at $\boldsymbol{r} = 0$. Various time delays give various displacements of this peak, by an amount $\delta \boldsymbol{r}$ which, together with δt, gives the plume velocity $\boldsymbol{v}_p$. The magnitude of $\boldsymbol{v}_p$ gives the plume speed s_p, and its direction is taken as the direction θ_p of the plume motion. Indeed, θ_p is seen to be close to the orientation of the long axis of the plume. This long-axis orientation tended to fluctuate about θ_p. It is assumed that the LSC orientation is the direction of the plume motion. Time series typically contained from 8200 to 20 200 images.

2.3.2. *Plume area-density measurements*

In order to determine the area density of plume ρ_p, a threshold equal to half the average intensity was applied to the background-subtracted images and all pixels with values above (below) the threshold value were set to zero (one). This isolated the warm plumes near the bottom plate, and the fraction of the pixels in the plume images (i.e. the fractional area occupied by their shadowgraph images) could be determined. This density was calculated using a central circular area of radius about half that of the cell as shown in figure 2(b), but the results were not very sensitive to the precise area chosen provided the annulus very near the sidewall (where there

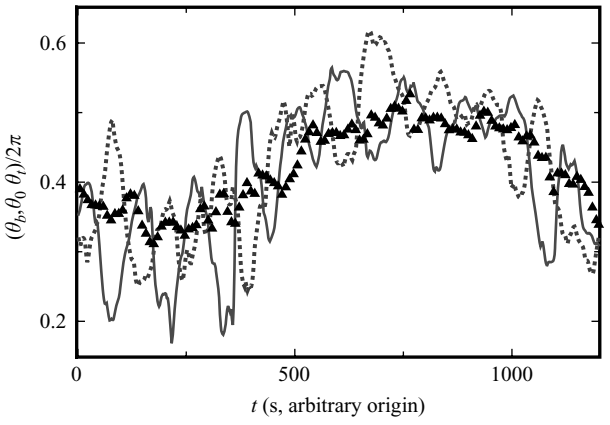

FIGURE 5. The large-scale-circulation orientations θ_b, θ_0, and θ_t calculated separately for the 3 sets of thermistors at $R = 3 \times 10^{10}$ in the large sample. Dotted line: θ_b from the bottom plane at a distance $L/4$ above the sample bottom ($z = -L/4$). Solid triangles: θ_0 from the mid-plane at a distance $L/2$ above the sample bottom ($z = 0$). Solid line: θ_t from the top plane at a distance $3L/4$ above the sample bottom ($z = L/4$). One can see that the top- and bottom-plane orientations oscillate, out of phase with each other, around the mid-plane orientation.

is an accumulation of many rising plumes) was excluded. Although ρ_p depended somewhat on the intensity cutoff, its time and Rayleigh-number dependence and its probability-distribution function showed no significant change over a wide cutoff range. As defined here, ρ_p can change either because plumes move into or out of the measurement area, or because the rate of plume generation changes; the measurement does not distinguish between these two processes.

3. Experimental results for aspect ratio $\Gamma = 1$

3.1. *Medium and large sample*

In the small sample, the frequency f_0 of temporal oscillations in the azimuthal direction of the motion of plumes across the bottom plate was previously observed using shadowgraphs (Funfschilling & Ahlers 2004). We can observe the same oscillations in the medium and large samples by looking at time series of the LSC orientations θ_t, θ_0, and θ_b at different heights. A short section of a much longer time series at the three heights is shown in figure 5 for $R = 3 \times 10^{10}$ in the large sample. While the orientation given by each data set contains erratic motion, there is a tendency for the orientations at the top and bottom planes to oscillate out of phase with each other around the mid-plane orientation.

Power spectra of the three time series for $\theta_i(t)$, $i = t, 0, b$ are shown in figure 6. Peaks representing oscillations are clearly seen for the top (θ_t) and bottom (θ_b) orientations, but for the mid-plane (θ_0) the spectrum gives no hint of oscillations. It is interesting to note that even a small misalignment of the sample relative to gravity, by 10^{-2} rad or less, will lead to oscillations also at the mid-plane. In several experiments by others the sample was deliberately tilted slightly in order to limit the diffusion of the LSC orientation to a small angular range, and caution is in order when results for the torsional mode are compared with measurements under those conditions. We have carried out an extensive study of the influence of a tilt angle on the LSC dynamics, and will report on this in a separate publication.

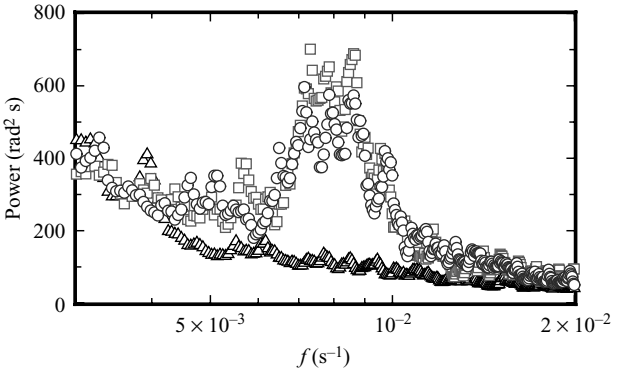

FIGURE 6. The smoothed power spectra of the three angles $\theta_i(t)$ for $R = 3 \times 10^{10}$ from the large sample. Triangles: θ_0. Circles: θ_t. Squares: θ_b.

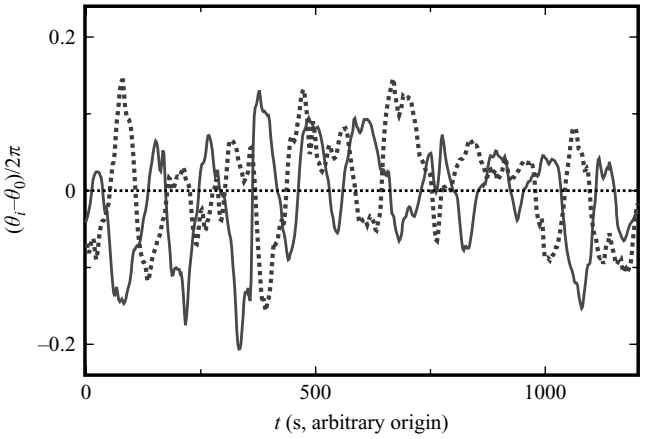

FIGURE 7. The large-scale-circulation orientations with the meandering of θ_0 subtracted out at $R = 3 \times 10^{10}$ in the large sample. Dotted line: $\theta_b - \theta_0$ from the bottom plane. Solid line: $\theta_t - \theta_0$ from the top plane. One can see that the top- and bottom-plane orientations oscillate, out of phase with each other, around the mid-plane orientation.

The oscillations of θ_b and θ_t about θ_0 are shown more clearly by the deviations $\theta_t - \theta_0$ and $\theta_b - \theta_0$ of the top- and bottom-plane orientations from the mid-plane orientation; these are shown in figure 7 for the data of figure 5. To reveal the nature of the oscillations more quantitatively, we compute the cross-correlation functions

$$g_{i,j}(\tau) = \langle [\theta_i(t) - \theta_0(t)] \times [\theta_j(t+\tau) - \theta_0(t+\tau)] \rangle \tag{3.1}$$

where i and j can each refer to either the top- or bottom-plane orientations θ_t or θ_b, and where $\langle ... \rangle$ without a subscript represents a time average. Normalized by $\sqrt{g_{i,i}(0) g_{j,j}(0)}$, these are shown in figure 8 for $R = 3 \times 10^{10}$ and the large sample. The oscillations in the auto-correlation functions confirm that the top- and bottom-plane orientations oscillate, and the lack of a large background in the auto-correlations confirms that the oscillation is really around the mid-plane orientation θ_0 and not around some fixed orientation. The cross-correlation similarly shows oscillations, and the minimum of $g_{t,b}(\tau)$ at $\tau = 0$ indicates that the top and bottom row oscillations are out of phase with each other by half a period. The oscillations shown here lead

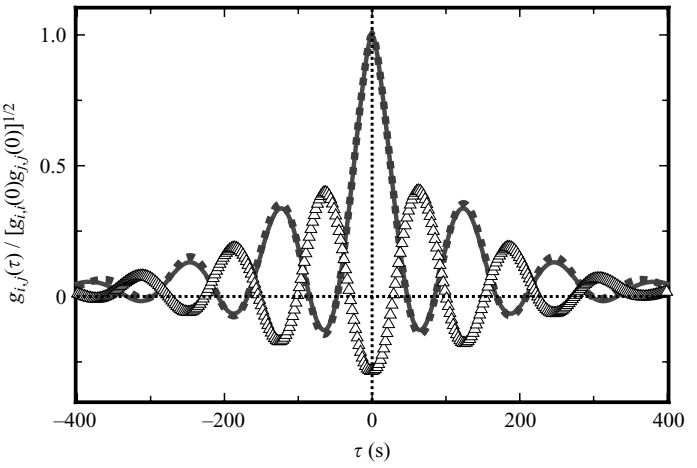

FIGURE 8. Normalized correlation functions $g_{i,j}(\tau)/\sqrt{g_{i,i}(0)g_{j,j}(0)}$ for the top-, mid-, and bottom-row LSC orientations for $R = 3 \times 10^{10}$. Open triangles: cross-correlation between top and bottom rows ($i = t$, $j = b$). Solid dots: auto-correlation of bottom row ($i = j = b$). Solid line: auto-correlation of top row ($i = j = t$). The oscillations are very clear, with the minimum of $g_{t,b}(\tau)$ at $\tau = 0$ indicating that the top- and bottom-plane orientations oscillate out of phase with each other.

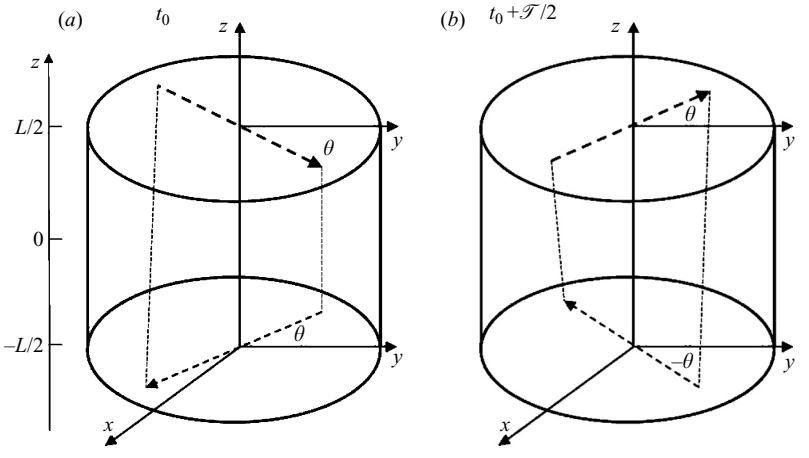

FIGURE 9. Schematic diagram of the LSC oscillation at time t_0 when the oscillation is at an extremum (a), and at time $t_0 + \mathscr{T}/2$ (i.e. half an oscillation period later) (b).

to the same picture of an azimuthal twisting, or torsional, oscillation of the LSC as found by Funfschilling & Ahlers (2004).

In figure 9 we show a schematic diagram that illustrates the nature of the oscillating mode, with the top and bottom out of phase. This mode can be described by

$$\theta(z, t) = \theta_0(t) + f(z)\theta'(t) \tag{3.2}$$

where $\theta(z, t)$ is the height-dependent orientation of the circulation plane of the LSC. If we choose the origin of the vertical axis at the horizontal mid-plane as shown in the figure, then the oscillation amplitude becomes an odd function of z, i.e. $f(z) = -f(-z)$. We set $f(L/4) = 1$ so that $\theta'(t) = \theta_i(t) - \theta_0(t)$ as shown in figure 7.

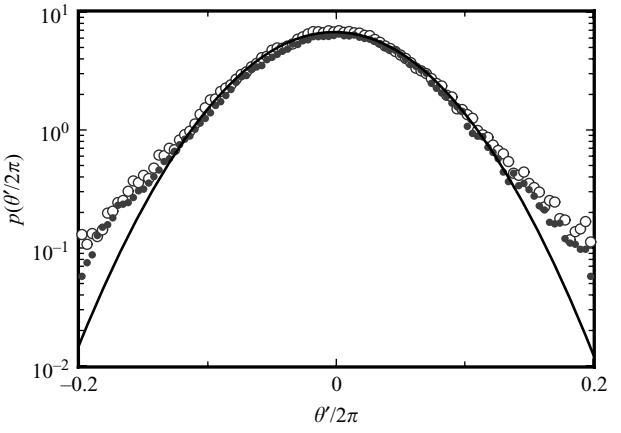

FIGURE 10. The probability distribution $p_{\theta'}$ for $\theta' = \theta_b - \theta_0$ (solid circles) and for $\theta' = \theta_t - \theta_0$ (open circles) for $R = 3 \times 10^{10}$ in the large sample. The solid line is a fit of a Gaussian function to the data near the peak. The fit gave a square root of the variance equal to 0.057, corresponding to about 20°.

Elsewhere we have shown that the background dynamics given by $\theta_0(t)$ is primarily diffusive, albeit interrupted by various relatively sudden re-orientation events (Brown *et al.* 2005*a*; Brown & Ahlers 2006*b*). The twist angle $\theta'(t)$ also has an irregular time dependence. In figure 10 we show the probability distribution $p_{\theta'}$ as a function of $\theta' = \theta_i - \theta_0$ with $i = t, b$. As shown by the solid line in the figure, the peak of $p_{\theta'}$ can be fitted well by a Gaussian function. Further away from the peak there are deviations from the Gaussian form, with the experimental data yielding a somewhat larger $p_{\theta'}$. If the twist could be represented by a simple oscillation with $\theta'(t) = A\cos(\omega t)$ with a constant (time-independent) A, then one would expect $p_{\theta'}$ to have maxima at $\theta' = \pm A$. In contrast to this, the measurements indicate a peak at $\theta' = 0$. This is consistent with a time-dependent $A(t)$ with a broad probability distribution p_A of A.

Recently Xi *et al.* (2006) studied the oscillations of the LSC circulation plane by particle-image velocimetry measurements in a horizontal plane located very near the top plate of their cylindrical sample with $\Gamma = 1$. They measured the peak-to-peak amplitude $2A(t)$ and found its average to be in the range from 35° to 55° with no clear dependence on R. Although they were not able to see the torsional nature of this mode by measurements at a single vertical position, they found a Gaussian-distributed $A(t)$. Their results for the time average $\langle A \rangle \simeq 22° \pm 5°$ of A are at least roughly consistent with our result for the square root of the variance of the azimuthal displacement θ', which we typically found to be near 20°.

A simple model for $\theta'(t)$ that reproduces a Gaussian $p_{\theta'}$ is given by the stochastic differential equation describing a damped driven harmonic oscillator

$$\ddot{\theta}' = -b\dot{\theta}' - \omega_0^2\theta' + g(t), \tag{3.3}$$

where b is a damping coefficient, ω_0 is the known angular oscillation frequency, and $g(t)$ is a Gaussian-distributed white-noise term. This equation produces oscillatory motion in appropriate parameter ranges, and it is known that diffusion in a harmonic well produces a Gaussian position distribution (Gitterman 2005). While we have no physical reason for using the model (3.3), it is similar in mathematical form to others used to describe the LSC dynamics (Brown & Ahlers 2006*a*, 2007, 2008). The orientation of the LSC has been found to have characteristics of diffusive meandering

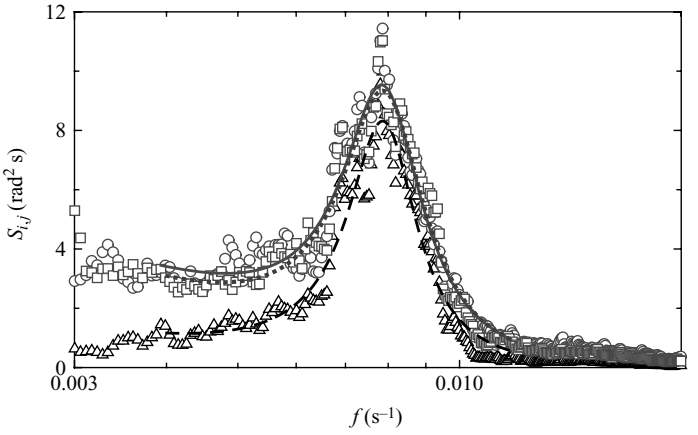

FIGURE 11. The smoothed power spectra $S_{i,j}(f)$ of θ' obtained from the Fourier transforms of each of the three correlation functions $g_{i,j}(\tau)$ for $R = 3 \times 10^{10}$ from the large sample. Triangles: $S_{t,b}$. Circles: $S_{t,t}$. Squares: $S_{b,b}$. Lines: a Lorentzian function with a exponential background is fit to the peak for $S_{t,b}$ (dashed line), $S_{t,t}$ (solid line), and $S_{b,b}$ (dotted line).

(consistent with Gaussian-distributed white noise for $g(t)$) both at the mid-plane (Brown & Ahlers 2006*a*; Sun *et al.* 2005*a*) and near the top plate (Xi *et al.* 2006). The good agreement between the predictions of the model (3.3) and the data for $p_{\theta'}$ indicates that the existence of the oscillatory mode is a result of the stochastic driving which we attribute to the small-scale turbulent fluctuations, and that this mode would decay without the driving.

The random time dependence of θ' also leads to the decay of the correlation functions shown in figure 8. In order to provide a quantitative characterization of $\theta'(t)$, we show a smoothed power spectrum (the square of the modulus of the Fourier transform, or the 'structure factor') $S_{i,j}(f)$ of $\theta_t - \theta_0$ and $\theta_b - \theta_0$ in figure 11. In addition, the Fourier transform of $g_{t,b}(t)$ is shown. Particularly for $S_{i,j}(f)$ one sees that there remain small backgrounds that are monotonically decreasing with f, although these backgrounds are much smaller than those seen in figure 6 for the spectra of θ_i. In addition to the background there is a strong peak at $f = f_0$ for all three spectra. Its finite width is attributable to the distribution of $A(t)$. We fitted an exponential background and a Lorentzian peak

$$S_{i,j}(f) = \frac{S_0}{1 + [(f - f_0)/\sigma_f]^2} + a \exp \frac{-f}{b} \tag{3.4}$$

to the data for $S_{i,j}(f)$ over the range $0.5 f_0 < f < 1.5 f_0$ with fitting parameters S_0, f_0, σ_f, a, and b. In figure 11 one sees that the Lorentzian shape gives a good representation of the data.

In figure 12 we show the Rayleigh-number dependence of the scaled (i.e. dimensionless) fit parameters $S_0 \nu / L^2$ (the peak height), $\sigma_f L^2 / \nu$ (the peak half-width), and $P_L = \pi S_0 \sigma_f$ (the total power under the Lorentzian peak excluding the background). The fit parameters for the bottom-plane, the top-plane and the cross-correlation data were quite similar, and thus in the figure their averages are displayed. One sees that the width of the peak increases and the height decreases with increasing R. For the dimensionless height the data from the two samples do not collapse onto a single curve, as would have been expected because the two samples have the same

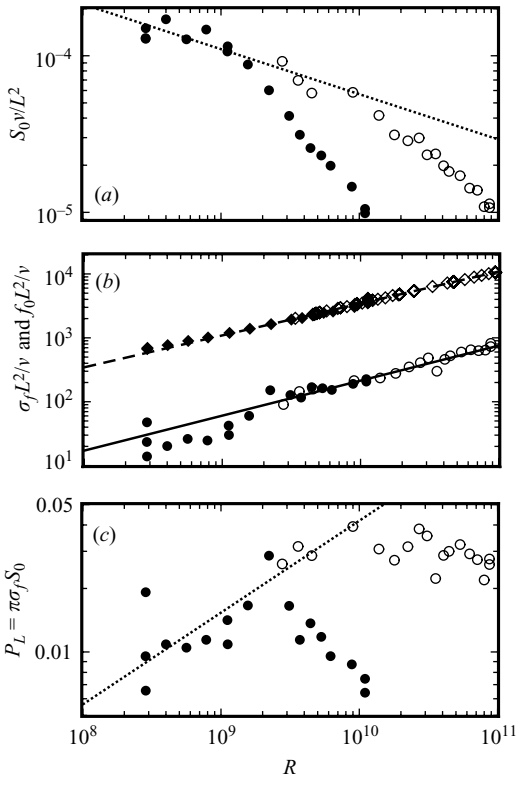

FIGURE 12. Fit parameters from (3.4) for the power spectra. These results are the averages obtained from the three spectra shown in figure 11. Solid symbols: medium sample. Open symbols: large sample. (*a*) Dimensionless peak height $S_0\nu/L^2$. The dotted line corresponds to a power law with an exponent of -0.45. (*b*) Dimensionless peak half-width $\sigma_f L^2/\nu$ (circles) and centre frequency f_0 (diamonds). The solid (dashed) line corresponds to a power law with an exponent of 0.55 (0.50). (*c*) The total power given by the area under the Lorentzian peak.

aspect ratio. It is not clear to us what physical phenomenon would produce this effect. Deviations from the Boussinesq approximation (Ahlers *et al.* 2006, 2007) which could influence the results at large R come to mind; however, for other properties such as the centre temperatures of the samples these effects come into play only at much larger values of the applied temperature differences. For the total power the R-dependences of S_0 and of σ_f partly cancel, yielding a power with only a weak dependence on R. As was seen for S_0, the data for the two samples do not collapse. The dimensionless half-width and centre frequency each fall on the same curve for the two samples, as one would expect for samples of the same Γ and σ. The centre frequency is closely related to the inverse turnover time, and thus the Reynolds number, of the LSC. This is discussed in detail elsewhere (Brown *et al.* 2007).

A question of interest is whether the LSC and/or its oscillations disappear at large R. As well as looking at the total power of the oscillations, one might consider the mode to be unresolvable when the width $2\sigma_f$ of the peak becomes significantly greater than the frequency f_0 of the mode, i.e. when the quality factor $Q = f_0/(2\sigma_f)$ becomes significantly less than one. This comparison can be made using the data for f_0 and σ_f in figure 12(*b*). A power-law fit to the half-width for $R > 3 \times 10^9$ yields $\sigma_f \propto R^{0.55}$,

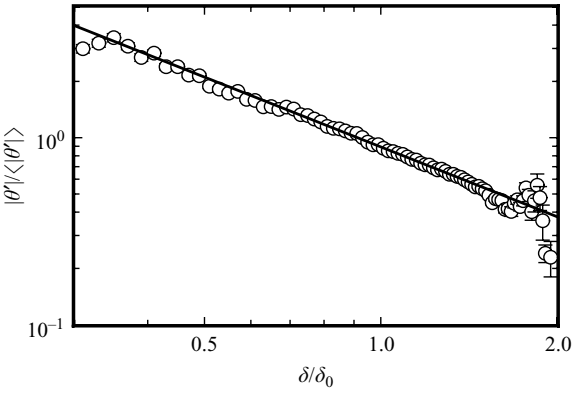

FIGURE 13. The time-average twist displacement θ' as a function of δ for $R = 3 \times 10^{10}$ in the large sample. Solid line: power-law fit to the data.

whereas such a fit to f_0 yields $f_0 \propto R^{0.50}$. In our range of R the half-width is about 1/10 of the frequency as seen in figure 11, i.e. $Q \simeq 5$. The closeness of the effective exponents for the two parameters implies that an extrapolation of the width to larger R remains small compared to the extrapolated frequency over a very large range of R, and thus that Q is nearly independent of R. This suggests that the torsional oscillation will not die out at any R obtainable in the laboratory owing to the spectral width becoming larger than the peak frequency unless the observed R-dependences change dramatically at higher R.

To gain some more insight into this mode, we bin the data based on the value of δ and plot the average magnitude of the twist displacement $|\theta'|$ as a function of δ at the mid-plane in figure 13. A power-law fit over the range $0.35 \leqslant \delta/\langle\delta\rangle \leqslant 1.9$ gives $|\theta'| \propto \delta^{-1.24}$. Since we do not find any corresponding oscillations in δ, this relationship indicates that the amplitude of oscillations in θ' decreases strongly with increasing δ. It suggests that this scaling law is similar to one found for the rotation rate $|\dot{\theta}_0|$ (Brown & Ahlers 2006*b*).

3.2. *Small sample*

3.2.1. *On the nature of plumes*

The nature of the relatively warm (cold) localized volumes of fluid, also known as 'plumes', that are emitted by the bottom (top) boundary layer has been investigated numerous times, in most cases by using the shadowgraph method. This method detects the integral along the path of observation of the refractive-index variations orthogonal to that path. When viewed from above (Tanaka & Miyata 1980; Zocchi, Moses & Libchaber 1990; Gluckman, Willaime & Gollub 1993; Verzicco 2002; Funfschilling & Ahlers 2004; Haramina & Tilgner 2004; Puthenveettil & Arakeri 2005; Zhou, Sun & Xia 2007) plumes have generally given the appearance of structures that are localized in only one horizontal direction and extended in an orthogonal horizontal direction. These structures often are referred to as 'sheet' plumes, although this term may be misleading because their two-dimensional extent does not seem to be established. We prefer to call them 'line' plumes because it appears more likely to us that they are one-dimensional excitations in the marginally stable boundary layers.

Examples of plume visualizations taken from above have been shown in figures 2 and 4. Four additional examples are shown in figure 14 for several values of R, and movies showing the dynamics for two of these examples are available with the online

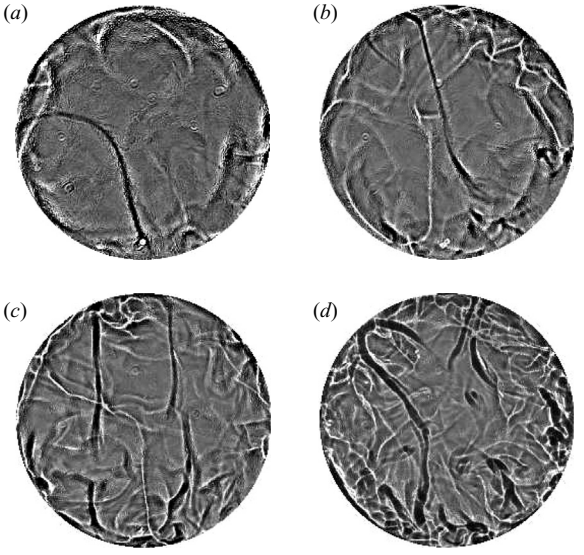

FIGURE 14. Shadowgraph images for the small $\Gamma = 1$ sample with methanol at a mean temperature of 40°C. (*a*) $R = 5.7 \times 10^7$. (*b*) $R, = 1.2 \times 10^8$. (*c*) $R = 2.3 \times 10^8$. (*d*) $R = 4.6 \times 10^8$. Movies corresponding to (*b*) and (*d*) are available with the online version of the paper.

version of this paper. A plume near the bottom plate appears as a narrow elongated relatively dark stripe. Since, to lowest order, the shadowgraph method under certain conditions yields the vertical average of the horizontal Laplacian of the refractive-index (and thus of the temperature) field (Rasenat *et al.* 1989; de Bruyn *et al.* 1996; Trainoff & Cannell 2002), such a dark stripe is generally framed on each side by an even more narrow light stripe. This entire structure then corresponds to a line plume. Analogous bright lines flanked by dark ones correspond to cold line plumes near the top, but in our work these were made less prominent by appropriate adjustment of the optics. Since the structure is viewed from above, we can have no direct information about its vertical extent. Thus, it could indeed be a sheet-like structure with significant vertical extent, or it could be a line structure with a predominantly horizontal orientation.

However, these structures are generally not observed in shadowgraphs taken in the horizontal direction (Zocchi *et al.* 1990; Moses *et al.* 1991; Moses, Zocchi & Libchaber 1993; Ciliberto *et al.* 1996; Zhang, Childress & Libchaber 1997; Du & Tong 1998; Qiu & Tong 2001*b*; Shang *et al.* 2003; Xi, Lam & Xia 2004), where plumes usually have the appearance of lines, often emanating from and extending away from the boundary layer and terminating in a mushroom-shaped cap. We shall refer to these structures as 'mushroom plumes'. Since line plumes do not appear in lateral observations, it appears that they are confined to the immediate vicinity of the bottom or top boundary layer where visualization from the side becomes difficult. The mushroom plumes are found in transverse observations primarily in the lower or upper portion of the sample, but often well separated from the bottom or top boundary layer. They are swept laterally by the LSC toward the sidewall. Near the sidewall they rise or fall owing to their buoyancy. From all of these observations the picture emerges that plumes are born as line excitations of the boundary layers, extended in one horizontal direction only and having initially very little if any vertical extent. These excitations are also swept laterally and in very close proximity to the

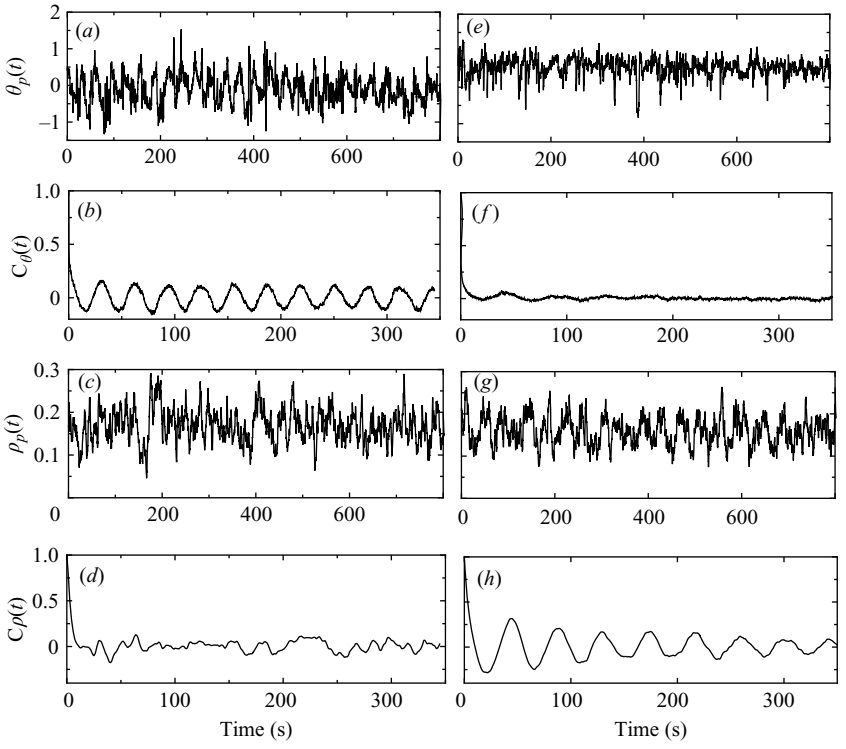

FIGURE 15. (*a*) The plume direction θ_p and (*c*) density ρ_p, and their correlation functions (*b*) $C_\theta(\tau)$ and (*d*) $C_\rho(\tau)$, as a function of time t or τ: $\Gamma = 1$ with 2-propanol and $R = 7.8 \times 10^8$. (*e–h*) corresponding plots for $\Gamma = 2$ with 2-propanol and $R = 1.5 \times 10^8$.

boundary layer by the LSC. In the presence of the LSC they orient themselves with their long axis in the direction of the LSC. This alignment phenomenon is well known in other contexts, where convection rolls align their axes with a prevailing wind or in the direction of a shear (for a review, see for instance Kelly 1994). At some point along their path, and especially when impinging upon the sidewall, line plumes separate from the boundary layer and evolve into mushroom plumes with their characteristic mushroom-shaped heads. This process leaves the sample centre relatively free of plumes. Consequently observations from the top and not too close to the sidewall reveal primarily the line plumes very near the top and bottom boundaries.

3.2.2. *Plume-direction oscillation and plume area density*

As reported before from experiments using methanol (Funfschilling & Ahlers 2004), the azimuthal direction $\theta_p(t)$ of the lateral motion of plumes near the top or bottom plate oscillates in time. This is illustrated in figures 15(*a*) and 15(*b*) for a Rayleigh number of 7.8×10^8 using 2-propanol as the fluid. Figure 15(*a*) gives a short segment of a much longer time series of $\theta_p(t)$. The signal is quite noisy because occasionally there are too few or no plumes present and the calculated cross-correlation function between successive images (see figure 4) does not reflect plume motion. Although an algorithm could have been developed to eliminate these spurious points, it turned out that the time correlation-function

$$C_\theta(\tau) = \langle \theta_p(t)\theta_p(t+\tau) \rangle_t \tag{3.5}$$

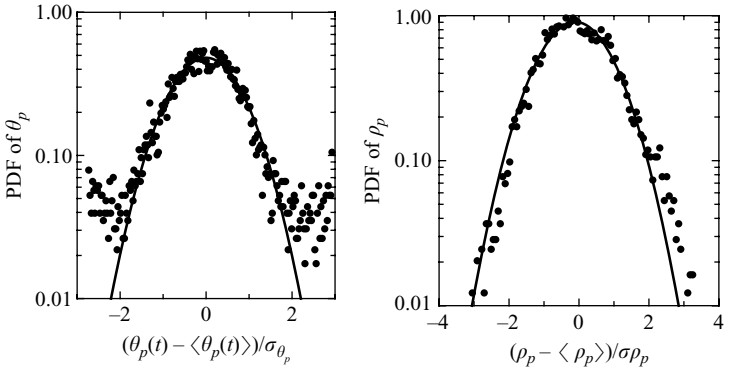

FIGURE 16. The probability-density functions (PDF) of θ_p and ρ_p for $\Gamma = 1$ and 2-propanol. The horizontal axes were scaled by the square roots of the variances σ_{θ_p} and σ_{ρ_p} of the data. The Rayleigh number was $R = 7.8 \times 10^8$. The solid lines are fits of a Gaussian function to the data.

shown in figure 15(*b*) clearly reveals the oscillations and shows that they remain coherent over a long time period. We assume that the plume motion is slaved to the motion of the LSC and that θ_p closely reflects the LSC flow direction $\theta(\pm L/2, t)$ (see (3.2)) near the top and bottom plates. The same oscillations have been found also in velocity measurements using air (Resagk *et al.* 2006) as the fluid. Simultaneous measurements for methanol using the top (bright) and bottom (dark) plumes revealed that the oscillations near the top and bottom plate are out of phase with each other by π (Funfschilling & Ahlers 2004), consistent with the sidewall-temperature measurements reported above in § 3.1 and shown in figure 8.

The results for θ_p lead to a power spectrum (not shown here) similar to those of θ_t and θ_b in figure 6, with a pronounced peak centred at a characteristic frequency f_0 which corresponds to the inverse turnover time of the LSC. The Reynolds numbers corresponding to f_0 already have been discussed by Brown *et al.* (2007).

The area density of plumes $\rho_p(t)$ is illustrated in figure 15(*c*). One sees that ρ_p varied irregularly with time, with no obvious oscillatory component. This is borne out by the time auto-correlation function of ρ_p, which is shown in figure 15(*d*) and which meanders non-periodically about zero.

In figure 16 we show the probability-density functions (PDF) of $\theta_p(t)$ and of the density $\rho_p(t)$ for the example of figure 15. These functions show an unremarkable Gaussian distribution. Such a distribution has been noted (Zhou *et al.* 2007) with regard to other features of plumes in turbulent RBC.

The oscillation amplitudes of θ_p can in principle be estimated from the power spectrum of θ_p in a manner similar to that employed to obtain the data in figure 12 for θ_t and θ_b. However, the signal-to-noise ratio was considerably smaller for this method than it was for the sidewall-temperature measurements, and no definitive statement about the Rayleigh-number dependence of the amplitude could be made. Thus we only mention that typical values were in the range from 0.3 to 0.7 rad for $5 \times 10^8 < R < 3 \times 10^9$, both for 2-propanol and for methanol.

4. Results for aspect ratios $\Gamma > 1$

For the aspect ratios $\Gamma = 2$ and $\Gamma = 3$ the oscillations of θ_b were very weak or absent entirely. This is illustrated in figure 15(*e–h*) for $\Gamma = 2$ and 2-propanol. Figure 15(*e*)

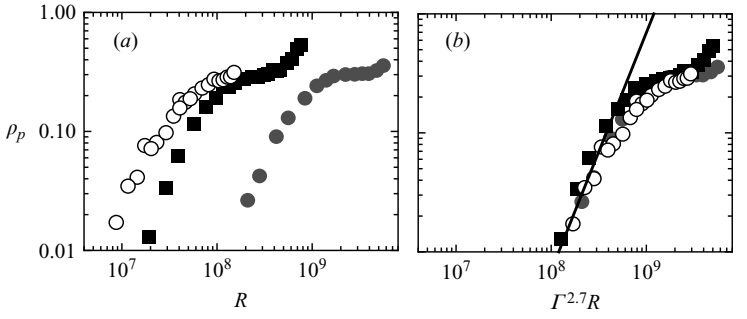

FIGURE 17. (*a*) The plume area-density above the bottom plate as a function of the Rayleigh number R. Solid circles: $\Gamma = 1$. Solid squares: $\Gamma = 2$. Open circles: $\Gamma = 3$. (*b*) The same data plotted as a function of $\Gamma^{2.7}R$. Solid line: a power law with an exponent of 2.0.

shows part of a time series of θ_p. No oscillations are apparent to the eye. Figure 15(*f*) gives the corresponding correlation function. Whereas it shows a hint of oscillations at early times, these decay within a few cycles. This stands in stark contrast to the $\Gamma = 1$ case where C_θ shows little or no decay over the time interval shown. On the other hand, for $\Gamma = 2$ the density of plumes (figure 15*g*) clearly oscillates. These ocillations are more clearly revealed by the correlation function in figure 15(*h*). This behaviour again stands in contrast to the $\Gamma = 1$ case where C_ρ showed no periodic component at all. The oscillations of ρ_p were found for all Rayleigh numbers above $R \simeq 2 \times 10^7$ for aspect ratio 2 and $R \simeq 1.5 \times 10^7$ for aspect ratio 3. The oscillation amplitudes of the densities were quite large (typically 50% of the mean value $\langle \rho_p \rangle$). In spite of the difference in the temporal structure between $\Gamma = 1$ on the one hand and $\Gamma = 2$ and 3 on the other, the PDFs of both θ_p and ρ_p were very similar for the two categories. We do not have any information about the geometrical features of the oscillating mode for the larger Γ cases. However, the difference presumably is associated with a major change in the structure of the flow.

Finally, in figure 17(*a*) we show the area density of the plumes above the bottom plate as a function of R for all three samples with 2-propanol. The data for the three aspect ratios fall on well separated curves. Interestingly, they essentially collapse onto a single curve when plotted against $\Gamma^{2.7}R$, revealing a strong Γ-dependence. A power-law scaling of ρ_p with R can be expected only when $\rho_p \ll 1$ because the density has an upper limit of unity by virtue of its definition. The R-range of the data over which $\rho_p \ll 1$ is rather small, and thus no effective exponent can be established with confidence. In addition the apparent plume width revealed by the shadowgraph method may depend on R. This effect would introduce an additional distortion of the measured R-dependence. As a guide to the R-dependence, the solid line in figure 17 is drawn with a slope of 2.

5. Summary and conclusions

In this paper we presented a detailed account of shadowgraph measurements, in part reported briefly before (Funfschilling & Ahlers 2004), of the azimuthal orientations θ_p of plume motions across the top and bottom plates of turbulent samples of fluid in cylindrical containers and heated from below. These data are for aspect ratios Γ from 1 to 3. It is argued that θ_p reflects the orientation of the LSC that is sweeping the plumes across the plates. For $\Gamma = 1$ the data revealed an azimuthal

LSC oscillation that had been shown before (Funfschilling & Ahlers 2004) to be a twisting mode of the LSC circulation plane, with the top and bottom halves oscillating out of phase by π. For $\Gamma = 2$ and 3 this mode was not present or extremely weak.

In addition to the results for θ_p, shadowgraph measurements for the plume area density ρ_p near the centre of the bottom plate are reported. For $\Gamma = 1$, ρ_p varied irregularly in time but did not reveal the oscillations found in θ_p. Interestingly, for the larger $\Gamma = 2$ and 3 (where θ_p did not oscillate) ρ_p had a strong oscillating component. The geometrical nature of the mode leading to an oscillation of ρ_p and only irregular meandering of θ_p is not yet revealed by the data.

For $\Gamma = 1$ the typical oscillation amplitude of θ_p was in the range from 0.2 to 0.7 rad. For all three aspect ratios, the shadowgraph measurements revealed that both ρ_p and θ_p had Gaussian probability distributions regardless of the absence or presence of oscillations. For small ρ_p (say $\rho_p \lesssim 0.2$) the plume area density for all three Γ had a strong Rayleigh-number dependence, but at large R ρ_p saturated near $\rho_p \simeq 0.4$ (we note that by virtue of its definition $\rho_p < 1$). There also was a strong Γ-dependence of $\rho_p(R)$. The data for all three Γ could be collapsed onto a unique curve when plotted against $\Gamma^{2.7\pm0.3}R$.

We also presented new measurements of the LSC orientation $\theta(z,t)$ by a very different method. These measurements are for two cylindrical samples with $\Gamma = 1$ over the Rayleigh-number range $10^8 \lesssim R \lesssim 10^{11}$ and for $\sigma = 4.4$. In this work we have determined $\theta_b = \theta(-L/4, t)$, $\theta_0 = \theta(0, t)$, and $\theta_t = \theta(+L/4, t)$ (we take the origin of the z-axis at the horizontal mid-plane) from measurements of the azimuthal dependence of the sidewall temperatures. The results confirm the shadowgraph observations in that they also show a torsional, i.e. twisting, mode of the LSC circulation plane, with $\theta_b(t)$ and $\theta_t(t)$ oscillating out of phase by π and θ_0 revealing no oscillatory contribution at all. Although each angle by itself shows a diffusive time evolution, with an oscillatory component added for θ_t and θ_b, the differences $\theta_i' = \theta_i - \theta_0$, $i = b, t$, reveal almost no meandering background at all, indicating that the oscillations are about θ_0 rather than about some other fixed angle.

For a purely sinusoidal oscillation of θ' with characteristic amplitude A one expects a probability distribution $p_{\theta'}$ of θ' that is strongly peaked near $\theta' = \pm A$. Instead, we found that $p_{\theta'}$ has a maximum at $\theta' = 0$ and that it has a Gaussian shape when $|\theta'|$ is not too large. This result is reproduced by the stochastic second-order differential equation that describes a damped harmonic oscillator driven by random noise. This equation for $\theta'(t)$ is reminiscent of the equations that we discussed elsewhere (Brown & Ahlers 2006*a*, 2007, 2008) to explain the rapid re-orientations of the LSC orientation and the influence of Earth's Coriolis force on the LSC. In those equations the physical origins of all terms were clear, and the small-scale turbulent background was represented by a phenomenological additive noise term corresponding to experimentally determined diffusivities. In the present case we assume that the required stochastic term likewise represents the background fluctuations, but we do not have a physical explanation for the origin of the inertial term that is needed in order to reproduce the oscillations. An important conclusion to be drawn from $p_{\theta'}$ is that the oscillations would not exist in the absence of the stochastic driving, and thus that they are not the result of a Hopf bifurcation of the deterministic system.

The oscillations of θ_b and θ_t lead to a peak at finite frequency of the power spectrum of $\theta_i - \theta_0$ ($i = t, b$), with only a small broad background contribution. The peak could be described by a Lorentzian function. We presented data for the height S_0, half-width σ_f, centre frequency f_0, and total power $P_L = \pi S_0 \sigma_f$ of this peak. We found that the

height S_0 of the peak decreased and that the width σ_f increased with increasing R. Although both f_0 and σ_f increase with R, the quality factor $f_0/(2\sigma_f)$ is nearly independent of R, suggesting that the oscillatory mode will survive up to R-values well beyond those of the present data unless a dramatic change in the behaviour of the system intervenes.

An interesting question is how the oscillatory mode comes into existence as R increases from small values. We do not have data at sufficiently small R to provide an answer, but this issue was addressed by Qiu & Tong (2001 *b*) using measurements at $\sigma = 5.4$. From velocity and temperature data at single points in the sample, and correlation functions between them, they found a sharp transition at $R_c \simeq 5 \times 10^7$ from a small-R state without coherent oscillations to another at larger R that exhibited the oscillations. At R_c the frequency observed by these authors had a finite value. Since we argued above that the oscillatory mode is not created via a Hopf bifurcation but instead is a consequence of the stochastic driving by the small-scale turbulent fluctuations, we interpret the observations of Qiu & Tong (2001 *b*) of a suden onset to imply that the driving begins abruptly as the Rayleigh number increases through R_c. Obviously, additional measurements will be required in order to clarify this important aspect of the LSC.

This work was supported by the US National Science Foundation through Grant DMR07-02111.

REFERENCES

Ahlers, G., Brown, E., Fontenele Araujo, F., Funfschilling, D., Grossmann, S. & Lohse, D. 2006 Non-Oberbeck-Boussinesq effects in strongly turbulent Rayleigh-Bénard convection. *J. Fluid Mech.* **569**, 409–445.

Ahlers, G., Brown, E. & Nikolaenko, A. 2005 Search for slow transients, and the effect of imperfect vertical alignment, in turbulent Rayleigh-Bénard convection. *J. Fluid Mech.* **557**, 347–367.

Ahlers, G., Fontenele Araujo, F., Funfschilling, D., Grossmann, S. & Lohse, D. 2007 Non-Oberbeck-Boussinesq effects in gaseous Rayleigh-Bénard convection. *Phys. Rev. Lett.* **98**, 054501.

Ahlers, G., Grossmann, S. & Lohse, D. 2002 Hochpräzision im Kochtopf: Neues zur turbulenten Konvektion. *Physik J.* **1** (2), 31–37.

Brown, E. & Ahlers, G. 2006*a* Effect of the Earth's Coriolis force on turbulent Rayleigh-Bénard convection in the laboratory. *Phys. Fluids* **18**, 125108.

Brown, E. & Ahlers, G. 2006*b* Rotations and cessations of the large-scale circulation in turbulent Rayleigh-Bénard convection. *J. Fluid Mech.* **568**, 351–386.

Brown, E. & Ahlers, G. 2007 Large-scale circulation model of turbulent Rayleigh-Bénard convection. *Phys. Rev. Lett.* **98**, 134501.

Brown, E. & Ahlers, G. 2008 A model of diffusion in a potential well for the dynamics of the large-scale circulation in turbulent Rayleigh-Bénard convection *Phys. Fluids* (in press).

Brown, E., Funfschilling, D. & Ahlers, G. 2007 Anomalous Reynolds-number scaling in turbulent Rayleigh-Bénard convection. *J. Statist. Mech.* P10005.

Brown, E., Nikolaenko, A. & Ahlers, G. 2005*a* Reorientation of the large-scale circulation in turbulent Rayleigh-Bénard convection. *Phys. Rev. Lett* **95**, 084503.

Brown, E., Nikolaenko, A., Funfschilling, D. & Ahlers, G. 2005*b* Heat transport in turbulent Rayleigh-Bénard convection: Effect of finite top- and bottom-plate conductivities. *Phys. Fluids* **17**, 075108.

de Bruyn, J. R., E. Bodenschatz, S. W. Morris, S. Trainoff, Y. Hu, Cannell, D. S. & Ahlers, G. 1996 Apparatus for the study of Rayleigh-Bénard convection in gases under pressure. *Rev. Sci. Instrum.* **67**, 2043–2067.

Castaing, B., Gunaratne, G., Heslot, F., Kadanoff, L., Libchaber, A., Thomae, S., Wu, X. Z., Zaleski, S. & Zanetti, G. 1989 Scaling of hard thermal turbulence in Rayleigh-Bénard convection. *J. Fluid Mech.* **204**, 1–30.

Ciliberto, S., Cioni, S. & Laroche, C. 1996 Large-scale flow properties of turbulent thermal convection. *Phys. Rev.* E **54**, R5901–R5904.

Cioni, S., Ciliberto, S. & Sommeria, J. 1997 Strongly turbulent Rayleigh-Bénard convection in mercury: comparison with results at moderate Prandtl number. *J. Fluid Mech.* **335**, 111–140.

van Doorn, E., Dhruva, B., Sreenivasan, K. R. & Cassella, V. 2000 Statistics of wind direction and its increments. *Phys. Fluids* **12**, 1529–1534.

Du, Y. B. & Tong, P. 1998 Enhanced heat transport in turbulent convection over a rough surface. *Phys. Rev. Lett.* **81**, 987–990.

Funfschilling, D. & Ahlers, G. 2004 Plume motion and large scale circulation in a cylindrical Rayleigh-Bénard cell. *Phys. Rev. Lett.* **92**, 194502.

Gitterman, M. 2005 *The Noisy Oscillator, The First Hundred Years, From Einstein Until Now*. World Scientific.

Glatzmaier, G., R. Coe, L. H. & Roberts, P. 1999 The role of the Earth's mantle in controlling the frequency of geomagnetic reversals. *Nature* **401**, 885–890.

Gluckman, B. J., Willaime, H. & Gollub, J. 1993 Geometry of isothermal and isoconcentration surfaces in thermal turbulence. *Phys. Fluids* A **5**, 646–761.

Haramina, T. & Tilgner, A. 2004 Coherent structures in boundary layers of rayleigh-bnard convection. *Phys. Rev.* E **69**, 056306.

Heslot, F., Castaing, B. & Libchaber, A. 1987 Transition to turbulence in helium gas. *Phys. Rev.* A **36**, 5870–5873.

Kadanoff, L. P. 2001 Turbulent heat flow: Structures and scaling. *Phys. Today* **54** (8), 34–39.

Kelly, R. E. 1994 The onset and development of thermal convection in fully developed shear flow. *Adv. Appl. Mech* **31**, 31–512.

Moses, E., Zocchi, G. & Libchaber, A. 1993 An experimental study of laminar plumes. *J. Fluid Mech.* **251**, 586–101.

Moses, E., Zocchi, G., Procaccia, I. & Libchaber, A. 1991 The dynamics and interaction of laminar thermal plumes. *Europhys. Lett.* **14**, 56–50.

Niemela, J., Skrbek, L., Sreenivasan, K. R. & Donnelly, R. J. 2001 The wind in confined thermal turbulence. *J. Fluid Mech.* **449**, 169–178.

Puthenveettil, B. A. & Arakeri, J. H. 2005 Plume structure in high-rayleigh-number convection. *J. Fluid Mech.* **542**, 212–749.

Qiu, X. L., Shang, X. D., Tong, P. & Xia, K.-Q. 2004 Velocity oscillations in turbulent Rayleigh-Bénard convection. *Phys. Fluids.* **16**, 412–423.

Qiu, X. L. & Tong, P. 2001*a* Large scale velocity structures in turbulent thermal convection. *Phys. Rev.* E **64**, 036304.

Qiu, X. L. & Tong, P. 2001*b* Onset of coherent oscillations in turbulent Rayleigh-Bénard convection. *Phys. Rev. Lett* **87**, 094501.

Qiu, X. L. & Tong, P. 2002 Temperature oscillations in turbulent Rayleigh-Bénard convection. *Phys. Rev.* E **66**, 026308.

Qiu, X. L., Yao, S. H. & Tong, P. 2000 Large-scale coherent rotation and oscillation in turbulent thermal convection. *Phys. Rev.* E **61**, R6075.

Rasenat, S., Hartung, G., Winkler, B. I. & Rehberg, I. 1989 The shadowgraph method in convection experiments. *Exps. Fluids* **7**, 412–420.

Resagk, C., du Puits, R., Thess, A., Dolzhansky, F., Grossmann, S., Fontenele Araujo, F. & Lohse, D. 2006 Oscillations of the large scale wind in turbulent thermal convection. *Phys. Fluids* **18**, 095105.

Sano, M., Wu, X. Z. & Libchaber, A. 1989 Turbulence in helium-gas free convection. *Phys. Rev.* A **40**, 6426–1430.

Shang, X. D., Qiu, X. L., Tong, P. & Xia, K.-Q. 2003 Measured local heat transport in turbulent Rayleigh-Bénard convection. *Phys. Rev. Lett.* **90**, 074501.

Siggia, E. D. 1994 High Rayleigh number convection. *Annu. Rev. Fluid Mech.* **26**, 137–168.

Sun, C., Xi, H. D. & Xia, K. Q. 2005*a* Azimuthal symmetry, flow dynamics, and heat transport in turbulent thermal convection in a cylinder with an aspect ratio of 0.5. *Phys. Rev. Lett.* **95**, 074502.

Sun, C., Xia, K. Q. & Tong, P. 2005*b* Three-dimensional flow structures and dynamics of turbulent thermal convection in a cylindrical cell. *Phys. Rev.* E **72**, 026302.

Takeshita, T., Segawa, T., Glazier, J. A. & Sano, M. 1996 Thermal turbulence in mercury. *Phys. Rev. Lett.* **76**, 1465–1468.

Tanaka, H. & Miyata, H. 1980 Turbulent natural convection in a horizontal water layer heated from below. *Intl J. Heat Mass Transfer* **23**, 1273–1281.

Trainoff, S. P. & Cannell, D. S. 2002 Physical optics treatment of the shadowgraph. *Rev. Sci. Instrum.* **14**, 1341–0363.

Tsuji, Y., Mizuno, T., Mashiko, T. & Sano, M. 2005 Mean wind in convective turbulence of mercury. *Phys. Rev. Lett.* **94**, 034501.

Verzicco, R. 2002 Sidewall finite conductivity effects in confined turbulent thermal convection. *J. Fluid Mech.* **473**, 201–210.

Xi, H. D., Lam, S. & Xia, K.-Q. 2004 From laminar plumes to organized flows: the onset of large-scale circulation in turbulent thermal convection. *J. Fluid Mech.* **503**, 47–56.

Xi, H. D., Zhou, Q. & Xia, K. Q. 2006 Azimuthal motion of the mean wind in turbulent thermal convestion. *Phys. Rev.* E **73**, 056312.

Xu, X., Bajaj, K. M. S. & Ahlers, G. 2000 Heat transport in turbulent Rayleigh-Bénard convection. *Phys. Rev. Lett.* **84**, 4357–4360.

Zhang, J., Childress, S. & Libchaber, A. 1997 Non-Boussinesq effect: Thermal convection with broken symmetry. *Phys. Fluids* **9**, 1034–1042.

Zhou, S. Q., Sun, C. & Xia, K. Q. 2007 Measured oscillations of the velocity and temperature fields in turbulent Rayleigh-Bénard convection in a rectangular cell. *Phys. Rev.* E **76**, 036301.

Zocchi, G., Moses, E. & Libchaber, A. 1990 Coherent structures in turbulent convection: an experimental study. *Physica* A **166**, 387–407.